

Cross-Modal Geometric Hierarchy Fusion: An Implicit-Submap Driven Framework for Resilient 3D Place Recognition

Xiaohui Jiang, Haijiang Zhu, Chadei Li, Fulin Tang, and Ning An

Abstract—LiDAR-based place recognition is critical for long-term autonomous driving without GPS. Existing handcrafted feature methods face dual limitations. First, descriptor instability occurs due to inconsistent point cloud density from motion and environmental changes during repeated traversals. Second, representation fragility arises from reliance on single-level geometric abstractions in complex scenes. To overcome these, we propose a novel framework for 3D place recognition. We introduce an implicit 3D representation using elastic neural points. This method is inherently resilient to variations in input density and yields uniformly distributed representations. From this, we derive occupancy grids and normal vectors. These enable the construction of fused descriptors that integrate complementary perspectives: macro-level spatial layouts from a bird's-eye view and micro-scale surface geometries from 3D segments. Extensive evaluations on diverse datasets (KITTI, KITTI-360, MuRan, NCLT) demonstrate state-of-the-art performance. Our approach achieves an optimal balance between accuracy, runtime efficiency, and map memory footprint. It exhibits exceptional resilience and scalability. The code will be released soon.

Index Terms—LiDAR, place recognition, Implicit Neural Representation, 3D descriptors

I. INTRODUCTION

PLACE recognition is the ability to identify previously visited locations in robotics and autonomous driving systems. It serves as a cornerstone for achieving long-term autonomy in transportation systems [1]. This capability is crucial for autonomous mobile robots to achieve precise and robust positioning in unknown environments [2]. Place recognition also has a wide range of applications. For example, it is used in loop closure detection for Simultaneous Localization and Mapping (SLAM) [3]–[5], map merging in large-scale scene mapping [6], and autonomous robot navigation [7], [8]. Light Detection and Ranging (LiDAR) can obtain accurate measurement results even under various lighting conditions, such as in darkness or when disturbed by strong light. As a result, LiDAR plays a crucial role in unmanned systems. Meanwhile, with the rapid development of autonomous and robotic driving systems, there is an increasing demand for LiDAR-based place recognition [9]–[12].

This work was supported in part by the National Natural Science Foundation of China (Grant No.62202468 and No. 92367111) and the Key Science and Technology Innovation Project of CCTEG (No. 2024-TD-ZD016-01, 2024-TD-MS017). (Co-corresponding author: Fulin Tang and Ning An)

Xiaohui Jiang and Haijiang Zhu are with the College of Information and Technology, Beijing University of Chemical Technology, Beijing 100029, China. (e-mail: 2023200772@buct.edu.cn, zhuhj@mail.buct.edu.cn)

Chadei Li and Fulin Tang are with the School of Artificial Intelligence, University of Chinese Academy of Sciences, Beijing 100190, China. (e-mail:lichadei2021@ia.ac.cn, fulin.tang@nlpr.ia.ac.cn)

Ning An is with the Research Institute of Mine Artificial Intelligence, China Coal Research Institute, Beijing 100013, China. (e-mail:ning.an@cctegbigdata.com)

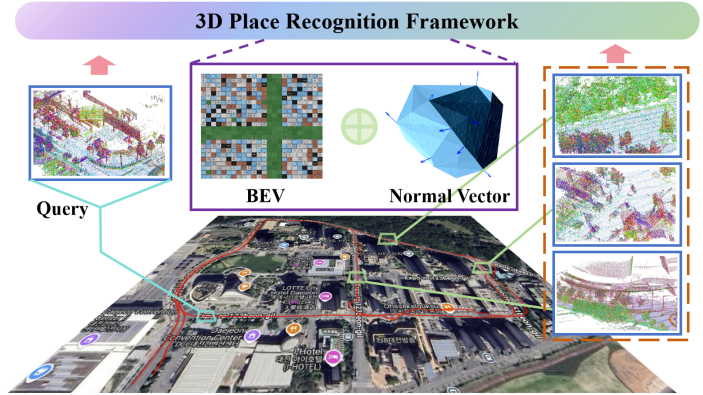


Fig. 1. Our 3D place recognition pipeline, unlike other methods, first converts the submaps into implicit neural point representations. The colored dots in the graph represent these neural representation points. Subsequently, utilizing the advantages of implicit representations, we fuse information from two modalities, namely BEV features and surface normal information of 3D segments, to generate descriptors for each submap.

In recent years, methods for place recognition based on LiDAR point clouds have developed rapidly. However, these methods still face several key challenges in practical applications:

- In urban environments, LiDAR point clouds from the same location often differ in density and coverage. These inconsistencies are due to variations in the trajectories and speeds of vehicles or robots. The algorithm, therefore, must be robust to such variability. It needs to maintain rotational and translational invariance, as well as invariance to point cloud density [13], [14].
- Dynamic objects in the scene, such as cars, pedestrians, and cyclists, constantly change the 3D structure of the environment. Their presence is unavoidable. This poses a challenge to the robustness of LiDAR point cloud-based place recognition [15], [16].

Most current hand-crafted feature extraction-based 3D place recognition methods follow two main strategies. One strategy extracts features (such as local features [17], [18] or global features [19], [20]) directly from the raw 3D point cloud. The alternative technique first transforms the point cloud into a structured format (for example, Bird's Eye View (BEV) [21], polar coordinate projections [22], intensity images [23], or sparse voxel grids [24]) before extracting features.

However, existing hand-crafted 3D feature extraction methods encounter a fundamental limitation: their dependence on narrow, single-modal scene representations. These methods typically

process either unstructured raw point clouds or a particular structured intermediate representation (e.g., BEV, Polar coordinates) derived from the point clouds. Critically, this reliance on any single representation fundamentally undermines feature robustness and coverage. Raw point clouds, although preserving exact geometric details, exhibit non-uniform spatial distributions (density variations) and lack intrinsic rotational and translational invariance, which hampers consistent feature extraction. In contrast, structured representations (e.g., BEV) enable concise global perspectives suitable for feature extraction, but they also forfeit detailed local geometry and vertical context, and perpetuate the point cloud's spatial irregularities. These inherited irregularities intensify the challenge of obtaining stable and discriminative features. Thus, features extracted solely from one modality remain insufficient for thorough and reliable 3D scene characterization, constraining downstream 3D place recognition performance.

To address these issues, we have moved away from the previous explicit 3D point cloud input and, instead, now use an elastic neural points-based implicit representation. This representation is introduced for three key reasons that are outlined below.

- The elastic neural points-based implicit representation is compact, flexible, and continuous. It possesses rotational and translational invariance, as well as spatial density invariance.
- This representation can efficiently provide high-quality, globally consistent surface normals, offering the opportunity to derive more discriminative place recognition descriptors.
- This representation enables more flexible online removal of dynamic objects, leading to more robust place recognition.

This paper proposes a novel hierarchical geometric fusion approach for LiDAR-based place recognition, as illustrated in Fig. 1. Our method uses a point-based implicit scene representation, combining Signed Distance Function (SDF) and stability prediction to filter dynamic objects online. We synergistically fuse macro-level Bird's-Eye View (BEV) descriptors, which capture global structural context, with micro-scale normal-based descriptors that encode distinctive local geometry. Specifically, features from BEV descriptors guide the identification and interpretation of salient local features, while the detailed information from normal-based descriptors refines and strengthens the BEV-based scene understanding. This bidirectional guidance enables each descriptor type to enhance the other's contribution, resulting in a robust and comprehensive scene descriptor that supports enhanced place recognition.

In summary, the contributions of this article are as follows:

- We introduce a point-based implicit representation. Its consistent properties and high-quality surface normals support a novel point cloud-based place recognition scheme.
- We propose a cross-modal geometric hierarchy fusion method that combines structural normal descriptors with rotation-invariant BEV features. This enables resilient

3D place recognition using complementary geometric representations.

- We propose a training-free, handcrafted feature extraction method. Our implicit representation saves storage and enables real-time operation. Extensive experiments show our method outperforms state-of-the-art approaches.

II. RELATED WORKS

In this section, we provide a comprehensive review of implicit map representation, as well as 3D point cloud place recognition methods based on both handcrafted and deep learning approaches.

A. Implicit Neural Map Representation

Explicitly represented maps (e.g., point clouds [27], meshes [28], voxel/occupancy grids [29], [30]) have been widely used in unmanned systems [25], [26]. Recently, implicit neural representations have demonstrated effectiveness in modelling radiation [31] and geometric fields [32], [33], enabling applications such as 3D reconstruction and novel view synthesis. Methods such as NeRF [31], DeepSDF [32], and occupancy networks [33] typically employ a single MLP to represent entire scenes. While effective, this approach faces efficiency bottlenecks (scalability, computation, and memory) in complex scenes. To address this, recent work has adopted hybrid representations that jointly optimize explicitly stored local latent features with shallow multilayer perceptrons (MLPs) [34]–[36].

Advances in efficient training now enable the scaling of implicit neural representations to larger scenes, accelerating their adoption in mapping and SLAM. For RGB-D SLAM, two main approaches exist for simultaneous scene modeling and camera pose tracking: one uses a single MLP to represent the entire scene as a global implicit function [37], [38], while the other uses grid-based local latent features with multiple shallow MLPs, enabling local modelling and improved scalability [39]–[41].

In addition to RGB-D approaches, LiDAR-based systems have also advanced, with methods like IR-MCL [42] and LocNDF [43] constructing implicit neural distance maps for robot localization. Building upon these developments, SHINE-mapping [44] extends implicit neural representations to large-scale outdoor LiDAR data using octree-based sparse voxel features for efficient storage. LONER [45] integrates incremental neural mapping with an ICP-based LiDAR odometry front-end for continuous scene updates. NeRF-LOAM [46] implements an online-optimizable octree feature grid, enabling efficient LiDAR odometry and mapping. PIN-SLAM [47] employs elastic neural points with hash-table indexing, significantly improving real-time performance and storage efficiency over previous neural mapping techniques. These LiDAR-based works demonstrate complementary advantages of implicit neural representations, including spatial continuity and rich feature encoding. Inspired by these distinctions, our method employs a point-based implicit neural representation. From this continuous representation, we directly derive scene surface normals and occupancy information, forming the essential basis for subsequent place recognition.

B. Handcrafted Methods

Early studies primarily described point clouds by extracting their geometric local features, including distance [48], point normal [49], angle [50], and density [51], among others. These methods have achieved success in point cloud registration and shape recognition. As research progressed, researchers began to encode the entire point cloud into a global feature descriptor. For example, Z-Projection [52] projects the point cloud onto a certain direction (such as the Z-axis), extracts angular and height information, and then calculates the similarity through the Sørensen distance or the Wasserstein distance. Similarly, Fast Histogram [53] utilizes a fast histogram to statistically analyze angular and height information, and evaluates similarity using the Wasserstein distance. Another approach, M2DP [54], projects the point cloud onto multiple two-dimensional planes, calculates the point density on each plane, and forms a signature vector. This method avoids calculating point normals, thereby improving computational efficiency; however, some information may be lost. In contrast, Scan Context [55], [56] divides the horizontal space into multiple annular regions and fan-shaped regions, forming a two-dimensional height matrix. By performing nearest neighbor search through the annular key and the similarity score, good results have been achieved. To further enhance performance, researchers have begun to combine other types of features, such as intensity [57] and spatial binary patterns [58], among others. For instance, LiDAR Iris [59] converts point cloud data into "iris images", generates binary signatures through the LoG-Gabor filter and threshold operations, and then calculates the similarity through the Hamming distance. In another direction, STD [18] proposes a stable triangle descriptor based on the invariance of the triangle shape. By extracting key points and encoding them into triangle descriptors, it enables efficient position matching and geometric verification. Additionally, BoW3D [82] employs an innovative bag-of-words model to process 3D LiDAR features. Finally, RING++ [83] constructs a rotation and translation invariant representation with strict mathematical guarantees by Radon transform, Fourier transform, and cross correlation, and solves the global localization problem on sparse maps.

Most handcrafted feature methods utilize a single modality (e.g., point clouds, voxels, BEV), resulting in information loss as cues from other sources are overlooked. While simple, these methods struggle with major rigid transformations or complex scenes. To address this, our approach uses an implicit neural point representation that combines 3D segment normals and BEV features. By hierarchically fusing these modalities, we build a more robust and comprehensive representation for challenging scenarios.

C. Learning-based Methods

PointNetVLAD [17] is a deep learning-based method that combines two crucial components: PointNet [60] and NetVLAD [61]. PointNet extracts features from point clouds. NetVLAD aggregates these local features into a 512-dimensional global descriptor. This method lays the foundation for subsequent approaches. Building on PointNetVLAD, two

methods—SOE-Net [62] and PCAN [63]—introduce attention mechanisms. These mechanisms dynamically emphasise the more important parts in the point cloud, enhancing the robustness of the descriptors. Locus [64] enhances the descriptors by introducing temporal information. This addition improves robustness against viewpoint changes. HiTPR [65] partitions the point cloud into dense voxels and uses a transformer network [66] to enhance correlation among local neighbours and dependency on global context. As a result, HiTPR demonstrates outstanding performance in highly complex and cluttered environments. Kim et al. [67] proposed a classifier based on a Convolutional Neural Network (CNN) for long-term place recognition. This approach can handle significant scene changes over an extended period. Semantic Scan Context [68] addresses the translation problem by introducing semantic information. LPD-Net [69] and vLPD-Net [70] use Graph Neural Networks (GNN) for feature aggregation. This enables them to capture geometric and shape characteristics of the point cloud effectively. DAH-Net [71] proposes a density-driven adaptive hybrid network using density changes of point clouds. It combines dynamic local feature aggregation with a contrastively enhanced linear attention module. With these, it attempts to address the challenges caused by density variations in point clouds from large-scale scenes. LCDNet [84] introduces a novel, unbalanced, optimal transport-based differentiable module. This module enables joint loop closure detection and 6-DoF pose estimation, allowing robust registration under arbitrary initial rotations and excelling at reverse loops. BEVPlace++ [85] introduces a Rotation-Equivariant Module (REM), enabling weakly supervised, real-time LiDAR global localisation. It extracts rotation-equivariant features from Bird's Eye View images, achieving robust 3-DoF pose estimation without precise ground truth. These learning-based methods often require relatively long training times and substantial computational resources. Moreover, they perform poorly when facing scenarios that fall outside their training samples.

III. METHOD

This section will introduce our proposed method for Lidar-based place recognition. In Section III-A, an overview of our method will be presented. Section III-B will demonstrate the elastic neural implicit representation. Section III-C and Section III-D will describe how we obtain hierarchy fusion descriptors with normal and BEV image information.

A. Overview

The main process of our proposed method is illustrated in Fig. 2. To better handle the random noise caused by variations in the density of point clouds (which refers to fluctuations in how densely the 3D data points, collected by sensors, are distributed in space) and by dynamic objects (objects in the environment that move or change over time), and to obtain more discriminative descriptors (distinctive features used to tell apart different parts of a scene), we use elastic neural implicit 3D points. This representation models the environment as a continuous field using a neural network, allowing for the

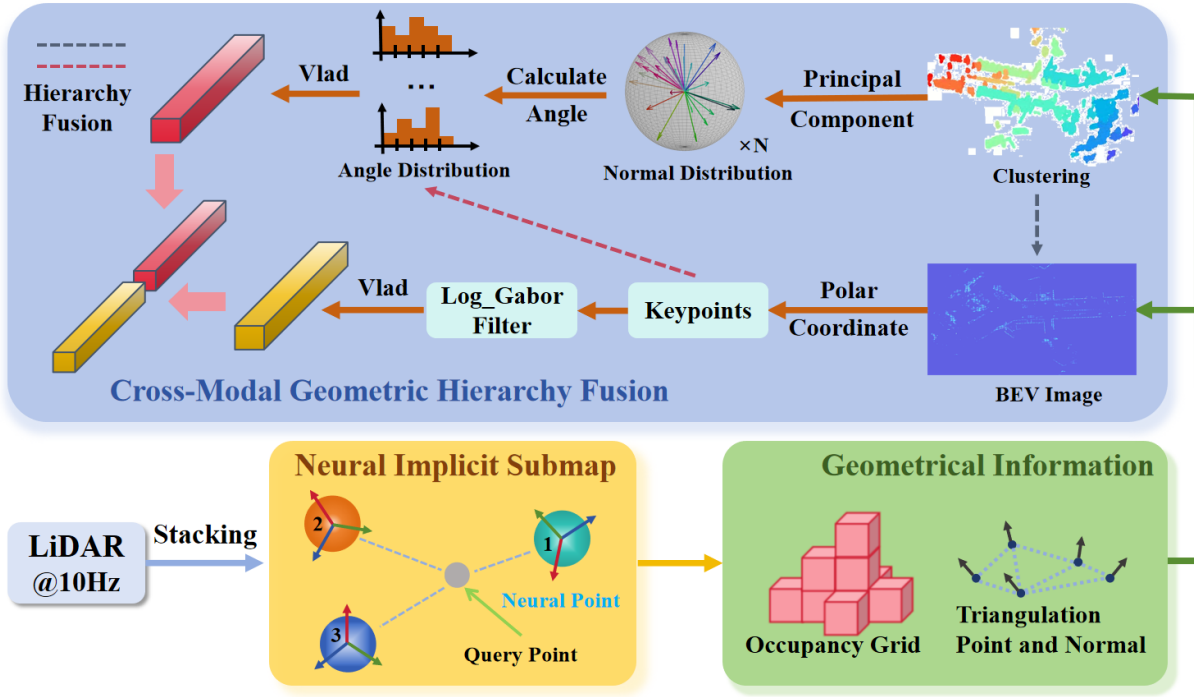


Fig. 2. This is the pipeline for our 3D Place Recognition. We feed a specific number of LiDAR frames to form a sub-map, which we then transform into an implicit neural point representation. From this, we derive high-quality occupancy grid information, triangular points, and normal vectors. BEV and primary 3D segments are obtained next. We use a log-Gabor filter to generate descriptors for the BEV, while the angular difference distribution of normal vectors yields geometric descriptors for the primary 3D segments. Finally, we combine these two descriptor types to form a single one for 3D place recognition. In the figure, yellow cuboids show macro descriptors from the bird's-eye view, and blue cuboids show micro descriptors from the main 3D segments. The two descriptors are hierarchically fused to integrate their advantages.

flexible positioning of points to more effectively describe the scene.

Because LiDAR (a technology that measures distances using laser light to produce detailed 3D maps) point clouds acquired in different scanning modes need to be processed, our method takes as input several frames of point clouds $\mathbf{P}_1, \dots, \mathbf{P}_n$, where each frame is a collection of 3D data points. The number n depends on the distance the robot has travelled, denoted by τ_n , which represents the path length corresponding to n frames.

Next, for the input sequence of point cloud frames, we utilise a point-based implicit representation to encode the scene's geometry. Starting from the first frame, the system generates samples (selected points) and labels (information or categories assigned to samples) to optimise the neural implicit map, which results in a sub-map (a smaller localised map) representation. We then extract from this implicit sub-map: the scene's occupancy grid (a division of space into a grid where each cell indicates occupancy), sample points (vertices of a generated mesh approximating surfaces), and surface normals (vectors perpendicular to the surface at each mesh vertex).

Then, we use Euclidean clustering (a technique that groups points based on how close they are to each other in 3D space) to quickly extract the main 3D segments of the scene. These segments guide the projection of the occupancy grid and the creation of the final bird's-eye-view (BEV) representation—a top-down 2D view of the 3D space. We detect keypoints

(distinct and important points in the data) on the BEV map, and calculate their spatial statistics (measures that summarise their distribution). These statistics provide initial information used to guide the extraction of feature descriptors (numeric vectors that describe local geometric properties) in the main 3D segments, thus generating a dense set of micro-scale surface signatures $\mathbf{F}^G \in \mathbb{R}^a$. Next, we aggregate the BEV-derived features using unsupervised clustering (a method to find groups in unlabeled data), to produce a compact BEV descriptor $\mathbf{F}^B \in \mathbb{R}^b$ that is highly distinctive. Finally, both descriptors are combined into a single fused feature representation $\mathbf{F}^{\text{fuse}} \in \mathbb{R}^{a+b}$.

B. Implicit Submap Representation With Elastic Neural Points

We will employ a memory-efficient implicit neural representation—a compact, learned model—to store the geometry of the sub-map. Based on elastic neural points (which means learned points that dynamically adjust), this representation possesses local rotational and translational invariance (remains the same when rotated or translated). Additionally, it is unaffected by the density of the original input point cloud (i.e., the number of points per space), has a uniform distribution (where points are spread out evenly), and can remove interference from certain dynamic objects (i.e., objects that move in the scene). Here, “elastic” signifies that the neural points undergo continual re-parameterisation: their 3-D positions and associated features are dynamically updated throughout sub-

map accumulation (as the map grows, both their positions and features change).

1) *Elastic Implicit Neural Point Cloud*: The results of the sub-map composed of neural implicit points \mathcal{M} are shown as follows:

$$\mathcal{M} = \{\mathbf{m}_i = (\mathbf{p}_i, \mathbf{q}_i, \mathbf{f}_i, t_i^c, t_i^u, \mu_i) \mid i = 1, \dots, N\} \quad (1)$$

Let $\mathbf{p}_i \in R^3$ and the quaternion $\mathbf{q}_i \in R^4$ represent the position and orientation of each neural point \mathbf{m}_i within the global coordinate frame, respectively. The optimizable latent feature encoding $\mathbf{f}_i \in R^F$ of each neural point serves to capture its local geometric characteristics. To efficiently track the state of every neural point, each \mathbf{m}_i retains a creation timestamp t_i^c , a last update timestamp t_i^u , and a stability metric μ_i .

2) *SDF Decoder*: The joint feature coordinate encoding for scene representation is employed to achieve fast convergence and reconstruct surface holes. To ensure invariance of the prediction to the local translation and rotation of neural points, the query position is transformed from the global frame to the local frame of each neural point. Specifically, let $\mathbf{d}_j \in R^3$ denote the query position in the local frame of neural point \mathbf{m}_j . This local coordinate \mathbf{d}_j is obtained by transforming the global coordinates \mathbf{p}_s of the query position using the pose of neural point \mathbf{m}_j , as follows:

$$\mathbf{d}_j = \mathbf{q}_j(\mathbf{p}_s - \mathbf{p}_j)\mathbf{q}_j^{-1}, j = 1, \dots, K \quad (2)$$

At the query position, \mathbf{p}_s , K nearby neural points are retrieved from the neural point map. For each neural point \mathbf{m}_j in the K -neighborhood \mathcal{N}_P , the coordinate is computed using the above Eq 2, and then the weight ω_j of each neural point is defined as:

$$\omega_j = \frac{\|\mathbf{d}_j\|^{-1}}{\sum_{k \in \mathcal{N}_P} \|\mathbf{d}_k\|^{-1}} = \frac{\|\mathbf{p}_s - \mathbf{p}_j\|^{-1}}{\sum_{k \in \mathcal{N}_P} \|\mathbf{p}_s - \mathbf{p}_k\|^{-1}} \quad (3)$$

Subsequently, the coordinate encoding $\mathbf{g}_i \in R^C$ of each neural point \mathbf{m}_j is defined as $\mathbf{g}_i = \gamma(\mathbf{d}_j)$, where $\gamma(\cdot)$ represents the positional encoding function. The feature encoding $\mathbf{f}_i \in R^F$ and coordinate encoding $\mathbf{g} \in R^C$ of the query point are derived by fusing the encodings of the nearest neighboring points along with their corresponding weights:

$$\mathbf{f} = \sum_{j \in \mathcal{N}_P} \omega_j \mathbf{f}_j, \mathbf{g} = \sum_{j \in \mathcal{N}_P} \omega_j \mathbf{g}_j \quad (4)$$

Finally, the neural decoder D_θ generates the SDF prediction s or the query position based on these encodings:

$$s = D_\theta(\mathbf{f}, \mathbf{g}) \quad (5)$$

D_θ is a shallow MLP containing M_{mlp} hidden layers with N_{mlp} neurons.

Upon acquisition of a fresh LiDAR point cloud, each point is examined for eligibility as a new neural point. A point is instantiated as a neural point only if one of the following two mutually exclusive conditions is satisfied: 1) The corresponding entry in the hash table retains its default value, indicating the absence of any previously stored neural point; a new neural point is then initialized. 2) The hash-table entry is occupied, yet the Euclidean distance between

the queried point \mathbf{p} and the stored neural point exceeds a predefined threshold, signifying a hash collision. In this case, the incumbent neural point is evicted and replaced by a newly initialized one.

We employ a dynamic point filtering method based on the stability μ_i and SDF values of neural points. A point is classified as a dynamic point and filtered if its SDF value exceeds a dynamic distance threshold γ_d and its stability value exceeds a stability threshold γ_μ . Specifically, a sampled point \mathbf{p}_w in the world coordinate system is considered dynamic if it satisfies conditions $\mathbf{S}(\mathbf{p}_w) > \gamma_d$ and $\mathbf{H}(\mathbf{p}_w) > \gamma_\mu$, where $\mathbf{S}(\mathbf{p}_w)$ represents the SDF value indicating the distance from the point to the nearest surface and $\mathbf{H}(\mathbf{p}_w)$ represents the stability value quantifying the consistency of the point across multiple observations. This method effectively removes dynamic objects from the map, enhancing its accuracy and consistency.

C. Normal Vector Descriptor

After getting the implicit submap representation, we extract the scene's occupancy, the mesh's points, and their normal directions.

To extract this information, the process begins by discretizing the submap into a voxel grid with a predefined resolution r . At each voxel corner point within this grid, we query the Signed Distance Function (SDF) value according to the method described previously. Based on these SDF values, we then apply an enhanced Marching Cubes (MC) algorithm to reconstruct a triangular mesh. This algorithm generates vertices uniformly distributed on the reconstructed surface. Subsequently, we calculate the normal vector for each vertex, defining the local surface orientation. To further refine the mesh, we filter the vertices to remove isolated outliers, thereby retaining only significant vertices along with their normals. Finally, by analysing the SDF values at the corners of each voxel, we derive occupancy information: voxels exhibiting a sign change in their corner SDF values are classified as occupied. This occupancy classification is essential for distinguishing between occupied and free space in the environment.

Subsequently, inspired by the work of FEC [72], [73], we apply a fast clustering method for mesh vertices. The algorithm is as **Algorithm 1**:

Following the derivation of clusters $\mathcal{C} = \{\mathbf{C}_1, \dots, \mathbf{C}_M\}$, points within each cluster are normalized. This normalization standardizes the scale of each cluster, thereby reducing sensitivity to noise and enhancing the robustness of subsequent geometric feature extraction. Specifically, all points in a cluster are isotropically scaled to be contained within a unit sphere of radius 1.

Following normalization, the next step involves partitioning the spherical domain into 72 sub-regions based on longitude and latitude. The sphere is first divided along the z-axis into northern and southern hemispheres. By latitude, each hemisphere is further divided into two bands, resulting in 4 latitude bands globally. Longitudinal division then subdivides each latitude band into 18 sectors, formed by meridians spaced 20 degrees apart. Fig. 3 illustrates this spatial subdivision.

Algorithm 1 Fast triangular Point Cloud Clustering

Require: mesh vertices point cloud **cloud**, minimum cluster size min_size , distance tolerance tol

Ensure: Cluster labels for each point

- 1: Build KD-tree **T** from **cloud**
- 2: $n \leftarrow |\text{cloud}|$
- 3: **if** $n < min_size$ **then**
- 4: **throw** "Point cloud too small"
- 5: **end if**
- 6: Initialize $labels[0..n - 1] \leftarrow 0$
- 7: $current_label \leftarrow 1$
- 8: **for** each point $p_i \in \text{cloud}$ **do**
- 9: **if** $labels[i] \neq 0$ **then**
- 10: **continue**
- 11: **end if**
- 12: $neighbors \leftarrow \mathbf{T}.\text{radius_search}(p_i, tol)$
- 13: **if** $neighbors$ is empty **then**
- 14: **continue**
- 15: **end if**
- 16: $min_tag \leftarrow \infty$
- 17: **for** each $j \in neighbors$ **do**
- 18: **if** $labels[j] > 0$ **then**
- 19: $min_tag \leftarrow \min(min_tag, labels[j])$
- 20: **end if**
- 21: **end for**
- 22: **if** $min_tag = \infty$ **then**
- 23: $min_tag \leftarrow current_label$
- 24: $current_label \leftarrow current_label + 1$
- 25: **end if**
- 26: **for** each $j \in neighbors$ **do**
- 27: **if** $labels[j] > min_tag$ **then**
- 28: **Relabel** all points with $labels[k] = labels[j]$ to min_tag
- 29: **end if**
- 30: $labels[j] \leftarrow min_tag$
- 31: **end for**
- 32: **end for**

Following the spherical partitioning, the mean normal vector is computed for each sub-region within a cluster. Next, the angular deviation between all unique pairs of these regional mean normal vectors within the same cluster is calculated. This process generates $\binom{n}{2}$ distinct angular measurements per cluster, where n is the number of sub-regions (e.g., $n = 72$). We then randomly select n_m measurements. A histogram of these angular deviations is constructed per cluster using 10-degree bin intervals, resulting in $d = 18$ dimensions. This process yields a d -dimensional geometric descriptor vector $\mathbf{F}_C \in \mathbb{R}^d$ for each cluster C .

Subsequently, for each 3D segment, the geometric descriptors \mathbf{F}_C from all its clusters are collected and normalised. The VLAD algorithm [74] is then applied to this normalised set of descriptors to generate a single submap-level geometric descriptor. To accommodate submaps with varying cluster counts (N_c), we dynamically adjust the size of the VLAD codebook (i.e., the number of cluster centres, K) during encoding, setting K proportionally to N_c . Submaps with a

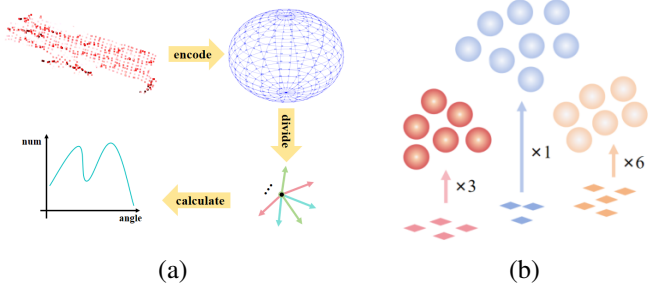


Fig. 3. (a) The figure illustrates the extraction of geometric descriptors for 3D segments. The input is a 3D segment with surface normals; color coding indicates normal deviations. First, these normals are mapped to discrete bins on a unit sphere, normalizing their distribution for systematic analysis. Then, the average angular deviation of the normals is calculated within each bin. Finally, these per-bin statistics are assembled into the geometric descriptors. (b) The figure illustrates the impact of keypoints on dominant 3-D segments, where diamond markers denote macro-level keypoints and colored spheres represent the distinct constituent points at the micro-level. The cardinality of keypoints assigned to each dominant segment subsequently governs the number of angular-distribution evaluations performed for that segment.

small N_c use a correspondingly smaller K , while those with a large N_c use a larger K . The resulting VLAD vector is then zero-padded to achieve a fixed dimensionality a . Finally, this yields the standardised geometric descriptor $\mathbf{F}^G \in \mathbb{R}^a$ for the submap. The entire process is illustrated in Fig. 3.

For each primary 3-D segment, we dynamically schedule the computation of micro-geometric descriptors. The number of evaluations depends on how many BEV feature points project into the segment. Specifically, the descriptor is computed between 1 and 10 times, using a linear mapping from the point count. Fig. 3 shows a diagram of this procedure. Details on BEV feature extraction are in Section III-D. Additionally, we adjust the computation frequency of the angular distribution for a segment based on the number of macro-level keypoints assigned to it. This design is motivated by observing that regions with many feature points often encode salient geometric structures. Allocating more computation to these regions yields more distinctive descriptors.

D. BEV descriptor

1) *Log-Gabor filters*: We project the acquired occupancy grid information onto the z-plane to obtain a BEV. During projection, we retain only points found near each dominant 3-D segment $C = \{C_1, \dots, C_M\}$. This effectively suppresses spurious and noisy observations. At an early and efficient clustering stage, road-surface points are discarded. We prune these because the implicit surface representation generates angular vertices that are sparsely scattered in geometrically impoverished regions. As a result, they fall below the saliency threshold and are removed during the clustering process. The size of each pixel in the BEV matches the physical size of the occupancy grids. Next, we normalise the pixel values of the input image to the range $[0, 255]$ to ensure numerical stability in subsequent processing. We then convert the input image's coordinates (u, v) into polar coordinates (ρ, θ) . Finally, we

construct a Log-Gabor filter [75], defined as follows:

$$L(f, \omega, s, o) = \exp\left(-\frac{(\log(f/f_s))^2}{2(\log(\sigma_f/f_s))^2} - \frac{(\omega - \omega_0)^2}{2\sigma_\omega^2}\right) \quad (6)$$

Among them, f_s and ω_o are the center frequency and direction of the filter, respectively. σ_f and σ_ω are the width parameters of the filter. Calculate each pixel point's filter responses at different scales and directions using the Log-Gabor filter. First, we perform the convolution operation, which involves convolving the filter with the input image:

$$A(\rho, \theta, s, o) = \|B(\rho, \theta) * L(\rho, \theta, s, o)\|^2 \quad (7)$$

Subsequently, for each direction o , the responses of all scales s are aggregated:

$$A(\rho, \theta, o) = \sum_s A(\rho, \theta, s, o) \quad (8)$$

The preset scale $s = 1, \dots, N_s$. s represents the scale index of the Log-Gabor filter.

2) *Maximum Index Map (MIM)*: MIM is an orientation map that records the direction of the maximum response of each pixel in all directions [76]. That is, for each pixel (ρ, θ) , find the direction o with the maximum response:

$$MIM(\rho, \theta) = \arg \max_o A(\rho, \theta, 0) \quad (9)$$

The size of the MIM is the same as that of the input image, and each pixel stores a direction index. Subsequently, the FAST corner detection algorithm is utilized on the MIM to extract key points. Subsequently, for each key point, we calculate the dominant direction around it. A MIM region of size $J \times J$ is taken around the key point, and an orientation histogram $\mathbf{h}(\mathbf{o})$ is constructed for this region to count the pixel values in each direction. Then, find the peak direction o_m of the histogram:

$$o_m = \arg \max_o \mathbf{h}(\mathbf{o}) \quad (10)$$

The main direction β is:

$$\beta = \frac{\pi o_m}{N_o} \quad (11)$$

Align the direction of the MIM region concerning the main direction to achieve rotational invariance, and rotate the MIM region by an angle of β .

$$patch_\beta(\rho, \theta) = \text{mod}(patch(\rho, \theta + \beta) - o_m, N_o) \quad (12)$$

The adjusted MIM region is partitioned into $l \times l$ sub-grids. A directional histogram is constructed for each sub-grid to count the pixel values in each direction. The histograms of all sub-grids are concatenated to form a feature vector. Finally, all the feature vectors are processed using the VLAD method to obtain the final BEV descriptor $\mathbf{F}^B \in \mathbb{R}^b$.

IV. EXPERIMENTAL RESULTS AND ANALYSES

In this section, Section IV-A describes the dataset selected by us and some experimental settings, Section IV-B introduces the evaluation metrics of the experiment, and Section IV-C presents the experimental results. Section IV-D and Section IV-E show the ablation experiment and running time and storage efficiency, respectively.

Dataset	KITTI	KITTI-360	NCLT	MulRan
LiDAR				
Velodyne HDL-64E	Velodyne HDL-64E	Velodyne HDL-64E	Velodyne HDL-32E	Ouster OS1-64
Field of View	$360^\circ \times 26.8^\circ$	$360^\circ \times 26.8^\circ$	$360^\circ \times 41.3^\circ$	$360^\circ \times 45^\circ$
No. of Sequences	6	4	6	9
Environment	Urban	Urban	Campus	Urban

Fig. 4. Datasets for experiment.

A. Dataset and Experimental Settings

Below, we provide a detailed description of the dataset used in this study. Our dataset includes various types of LiDAR and different application scenarios. The configuration of the LiDAR sensors used in this dataset is shown in Fig. 4.

- 1) *KITTI Dataset* [77]: This dataset was collected at 10 Hz in an urban environment using a mechanical LiDAR (Velodyne HDL-64E) mounted on top of a vehicle. We selected six sequences (00, 02, 05, 06, 07, 08) containing loop closure points for our experiments.
 - 2) *KITTI-360 Dataset* [78]: This dataset was also collected at 10 Hz in an urban scenario using a LiDAR (Velodyne HDL-64E). We selected four sequences (00, 04, 05, 06) containing loop closure points for the experiment.
 - 3) *NCLT Dataset* [79]: This dataset was collected using a 32-line LiDAR (Velodyne HDL-32E) mounted on a Segway robot. It was primarily collected on the University of Michigan campus, capturing variations across the four seasons, differing lighting conditions, and dynamic objects. Based on loop closure availability, we selected four sequences for the experiment: 2012-05-26 (NCLT01), 2012-08-20 (NCLT02), 2012-09-28 (NCLT03), and 2013-04-05 (NCLT04). Additionally, sequences 2012-03-17, 2012-02-04, and 2012-08-20 were used for cross-temporal location recognition experiments.
 - 4) *MulRan Dataset* [80]: This dataset contains data collected from multiple scenarios in South Korea using an Ouster OS1-64 LiDAR. We selected sequences 01 and 02 from the DCC, KAIST, and Riverside scenes for the experiment; these were labeled MulRan01 to MulRan06, respectively (e.g., DCC01=MulRan01, DCC02=MulRan02, etc.). Additionally, sequences Sejong01 to Sejong03 were used to conduct cross-temporal location recognition experiments.
- Our feature extraction method is manually applied to the sub-maps derived from the accumulated point clouds. To benchmark our approach, we selected five handcrafted feature extraction methods for comparison. These were evaluated on the selected datasets. The methods are Scan Context++ [56], M2DP [54], NDT [81], BoW3D [82], Ring++ [83], and STD [18]. M2DP, NDT, BoW3D, and STD can be applied directly to the accumulated sub-maps. To ensure a fair comparison, we also applied the Scan Context++ and Ring++ methods to the sub-maps. For this purpose, we re-projected the accumulated sub-map points onto the middle frame of the sub-map. This step simulated a dense "scan" captured from

that pose. BoW3D’s default configuration targets the KITTI dataset; therefore, we conducted our experiments only on the KITTI and KITTI-360 datasets. Ring++’s default configuration is tailored to the NCLT and Mulran datasets; therefore, we used those datasets exclusively for Ring++. All experiments were conducted on a laptop equipped with an Intel Core i7-10875H CPU at 5.10 GHz and 16GB RAM. We utilized an RTX 2060 GPU for acceleration during the construction of the neural implicit representations. The parameter values used in our method are listed in Table I.

TABLE I
PARAMETERS OF OUR METHOD

Parameter	Value	Description
τ_n	25 m	Movement distance to form a submap
K	8	Neighborhood neural point number
γ_d	$0.006r_{max}$	Dynamic filtering threshold for SDF
γ_μ	4	Dynamic filtering threshold for stability
M_{nlp}, N_{nlp}	8	MLP level and neuron count
r	0.2	Voxel resolution
min_size	200	Minimum number of clusters
$l \times l$	6×6	Number of subgrids
J	96	Local patch size
n_m	400	Number of angle differences
N_s	4	Number of scales of Log-Gabor filter

B. Performance Evaluation Metrics

In this article, the conditions for establishing a loop closure are defined as follows. For a query sub-map, first compute the average position of all its frames to represent the sub-map’s position. If the distance between this position and that of a previous sub-map is less than or equal to 20 meters, and their indices differ by more than 50, then these two sub-maps are considered positive (loop closure) pairs. The 20-meter distance threshold was chosen based on the urban environment, the typical range of LiDAR sensors, and the overall scale. Each method outputs a candidate frame with its similarity score and compares the score to a predefined decision threshold. If the score exceeds the threshold, classify the match as positive; if not, classify it as negative. For a match classified as positive, compute the actual geometric distance between the query frame and the candidate frame. If this distance is less than 20 meters, it is considered a true positive (TP); otherwise, it is classified as a false positive (FP). For a match classified as negative, if no ground truth loop closure exists for the query frame (according to the above criteria), it is considered a true negative (TN). If a ground truth loop closure exists for the query frame, it is a false negative (FN).

The following is how the evaluation metrics we adopt are calculated:

- 1) *Precision-Recall Curve*: In the field of place recognition, precision is defined as the ratio of true positive results to the total number of identified matches. Recall, in contrast, represents the ratio of true positive results to the total

number of actual positive instances. These concepts can be formally expressed as:

$$Precision = \frac{TP}{TP + FP} \quad (13)$$

$$Recall = \frac{TP}{TP + FN} \quad (14)$$

Here, TP denotes the number of true positive outcomes, FP represents the number of false positive results, and FN indicates the number of false negative instances. The precision-recall curve is constructed by adjusting decision thresholds. Each point on this curve corresponds to a specific threshold setting, illustrating the precision-recall trade-off and visually demonstrating how these metrics covary with threshold adjustments.

- 2) *AUC*: The Area Under the Curve (AUC) measures the area under the Precision-Recall (PR) curve. It is a common metric for checking model performance at different thresholds. AUC is a single number between 0 and 1. A higher AUC indicates that the model is more effective at identifying positive cases across various thresholds.
- 3) *Max F1 Score*: The F1 score, calculated using Eq 15, represents the harmonic mean of precision and recall. This score provides a balanced measure by combining both metrics. The Maximum F1 score acts as a comprehensive performance indicator. It is often used to identify the optimal decision threshold. By balancing the competing demands of precision and recall, it effectively reconciles these priorities. The peak F1 score value reflects the algorithm’s optimal performance. It demonstrates a balance between accurately identifying true positives and minimizing false positives.

$$F_1 = 2 \times \frac{Precision \times Recall}{Precision + Recall} \quad (15)$$

C. Experiment Performance Comparisons

To comprehensively test our method, we evaluated its performance in two major scenarios: short-term and long-term relocalization. Here, "short-term" refers to real-time detection of loop closure points. "Long-term" is the ability to recognize locations when revisiting the same area after more than one day. We further benchmark our approach against several learning-based counterparts. Our method ingests sub-maps accumulated from multi-frame point clouds. In contrast, most learning-based techniques operate on single-frame inputs. Therefore, we conduct the comparison under explicitly aligned data regimes to ensure fairness. For a rigorous comparison, we re-formulate the learning-based baselines (LCDnet [84], Bevplace++ [85]) so they ingest multi-frame inputs generated under the same conditions as our method. We adjust the temporal window and voxelization parameters so the tensors are shape-compatible with the pre-trained weights. This enables direct evaluation without retraining.

- 1) *short-term*: The PR curves for our proposed method and existing methods are shown in Fig. 5. We compared a total of 20 trajectories. Our method demonstrates superior performance compared to the existing methods. In the KITTI00 sequence,

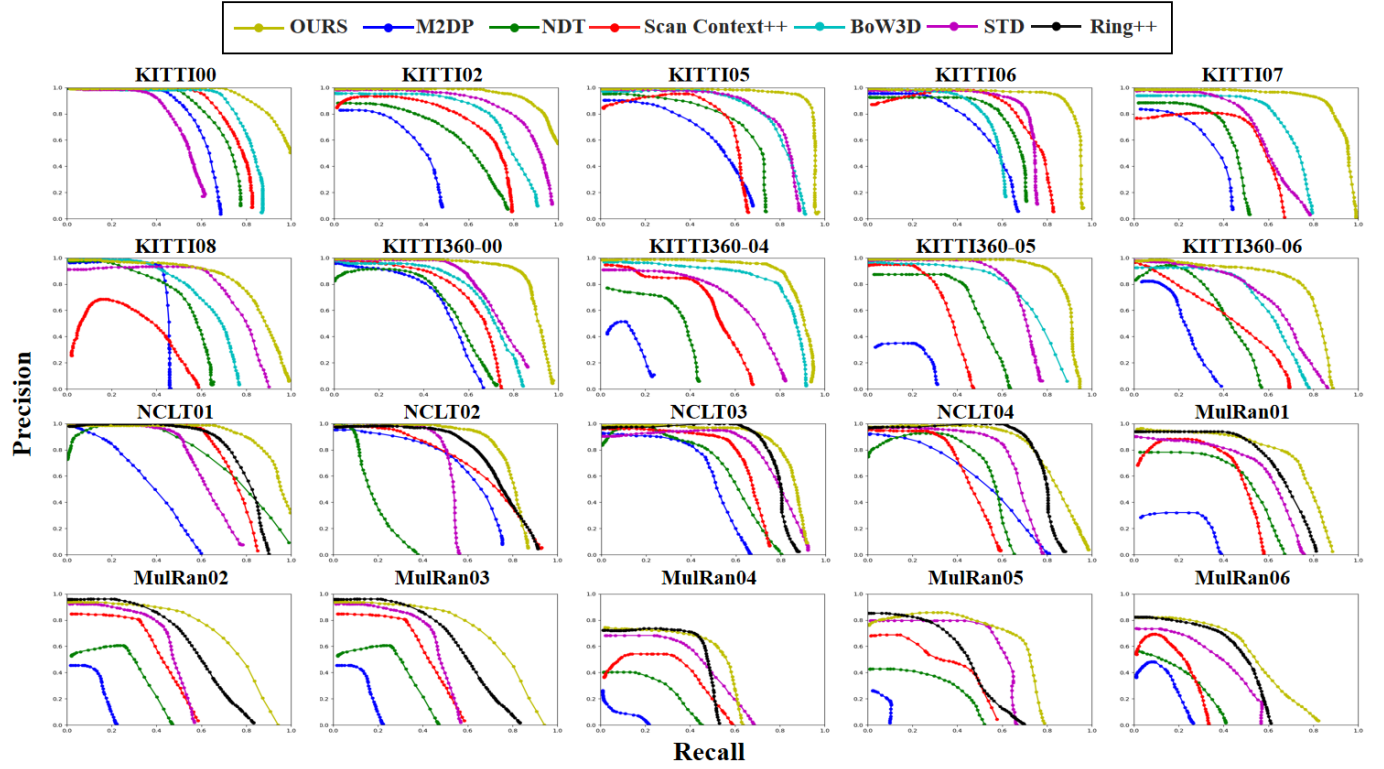


Fig. 5. Evaluation of twenty short-term sequences reveals that each subfigure in Figure 5 corresponds to the precision-recall performance of a specific method on these sequences. Our approach consistently outperforms all others across these sequences, demonstrating its robustness and adaptability. All image coordinates (x, y) are normalized to the unit interval $[0, 1]$, and the subsequently figure PR curves adhere to the same convention.

TABLE II
COMPREHENSIVE PERFORMANCE EVALUATION ACROSS MULTIPLE DATASETS (AUC \uparrow / MAX F1 SCORE \uparrow)

Method	KITTI				KITTI-360			
	00	02	05	06	00	04	05	06
M2DP	0.64/0.65	0.31/0.45	0.55/0.47	0.52/0.58	0.48/0.56	0.08/0.23	0.09/0.28	0.18/0.31
NDT	0.69/0.70	0.52/0.59	0.61/0.67	0.60/0.68	0.51/0.57	0.26/0.44	0.44/0.56	0.39/0.48
SC++	0.72/0.75	0.63/0.67	0.55/0.65	0.69/0.73	0.61/0.64	0.58/0.47	0.35/0.45	0.42/0.48
BoW3D	0.78/0.80	0.74/0.74	0.78/0.76	0.55/0.63	0.67/0.68	0.79/0.80	0.71/0.70	0.57/0.62
STD	0.51/0.58	0.85/0.80	0.78/0.76	0.71/0.77	0.71/0.71	0.60/0.64	0.68/0.71	0.63/0.64
Ours	0.93/0.86	0.95/0.88	0.93/0.91	0.91/0.89	0.89/0.86	0.87/0.85	0.87/0.86	0.76/0.77
Method	NCLT				MulRan			
	01	02	03	04	01	02	03	04
M2DP	0.37/0.44	0.58/0.62	0.47/0.57	0.49/0.53	0.10/0.30	0.07/0.21	0.10/0.23	0.02/0.10
NDT	0.75/0.69	0.18/0.26	0.57/0.61	0.51/0.61	0.41/0.55	0.21/0.38	0.17/0.34	0.13/0.30
SC++	0.74/0.74	0.67/0.64	0.63/0.69	0.44/0.52	0.41/0.55	0.36/0.48	0.34/0.48	0.24/0.42
STD	0.61/0.65	0.51/0.62	0.74/0.75	0.64/0.70	0.55/0.62	0.43/0.55	0.36/0.50	0.34/0.48
Ring++	0.78/0.77	0.72/0.71	0.77/0.79	0.77/0.79	0.63/0.66	0.57/0.59	0.42/0.53	0.35/0.53
Ours	0.92/0.85	0.77/0.78	0.83/0.81	0.82/0.78	0.70/0.73	0.70/0.69	0.50/0.58	0.40/0.56

Note: This table presents the Area Under the Curve (AUC) and maximum F1 scores for all evaluated methods across multiple datasets. The best result for each dataset is highlighted in bold.

there are only small rotational and translational changes when passing through the same location, so most methods perform well. In contrast, scenarios with significant rotational and translational changes at the same location (such as KITTI05, KITTI08, KITTI360-04, and KITTI360-05) cause existing

methods to generate inaccuracies. Our method retains robust performance in these cases. When there are numerous similar or repetitive scenes or when revisiting the same location multiple times, as in the six sequences in the MulRan dataset, all methods show some susceptibility to these challenging

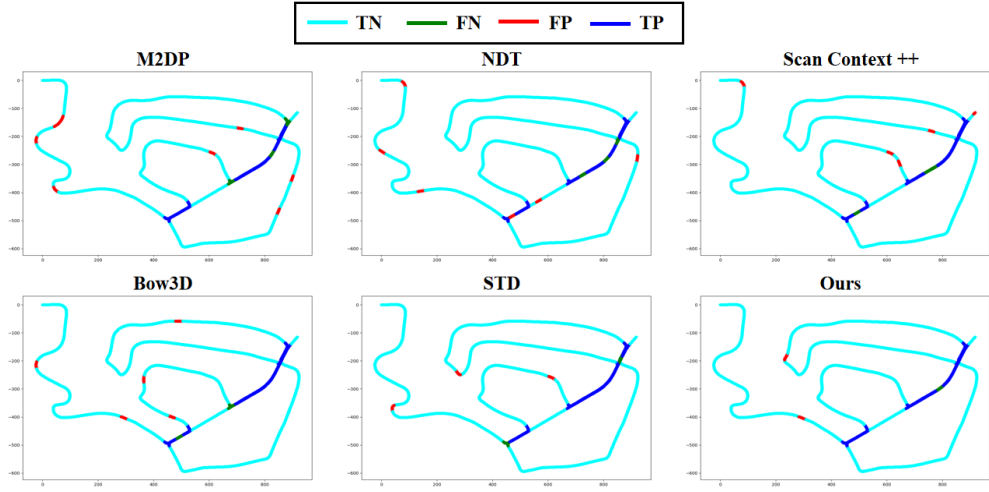


Fig. 6. Loop retrieval result using each method's max F1 score threshold on KITTI02.

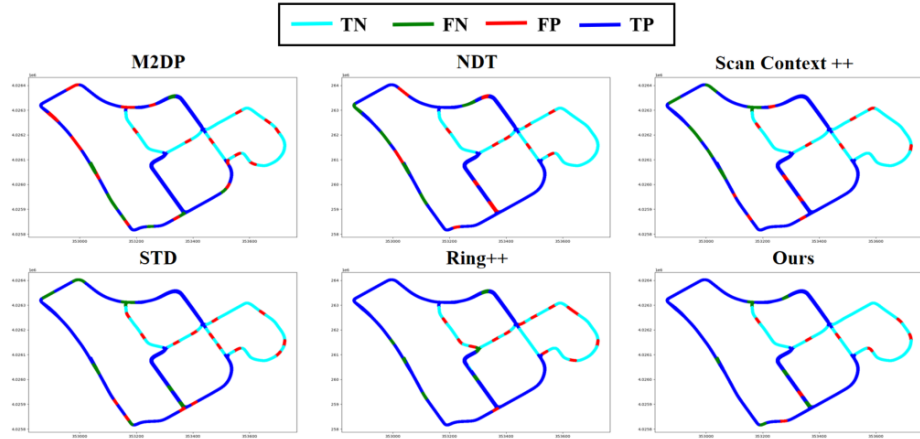


Fig. 7. Loop retrieval result using each method's max F1 score threshold on MulRan04.

conditions. Nevertheless, our method still maintains good performance. Table II presents the AUC values and peak F1 scores. Our method surpasses the compared approaches. Two sets of sequences for testing are presented in the figure to provide a detailed analysis of each method. All methods display their optimal performance, which is indicated by the maximum F1 score. Compared to other methods, ours achieves higher True Positives (TP) and lower False Positives (FP) and False Negatives (FN). To further highlight the distinction, we selected KITTI02 and MulRan04 tracks. We visualized their place recognition results, including TP, FP, FN, and TN, based on each method's optimal F1 score threshold. As shown in Figs. 6 and 7 show that our approach generates fewer false matches and detects loopback points more effectively. This delivers superior performance.

2) *long-term*: A robust place recognition system should perform reliably despite long-term environmental variations. To evaluate long-term place recognition performance, multiple intermittent datasets covering the same area were selected as the map sequence and query sequence, respectively. The results of our recall-precision experiments are shown in Fig. 8.

AUC and F1 scores are presented in Table III. Our method demonstrates superior performance across all metrics. Although performance declines compared to short-term experiments on the same dataset, this decline is largely attributed to increased retrieval scope and significant environmental changes over time, such as seasonal differences, lighting shifts, or structural modifications. These factors make the long-term place recognition task more complex.

3) *learning-based*: Although our framework leverages a learned implicit representation, the descriptor itself is constructed in a fully heuristic manner. This obviates the need for place-recognition labels and eliminates any training overhead. Nonetheless, to situate our approach within the state of the art, we benchmark it against leading learning-based baselines. The resulting PR curves are reported in Fig. 9. LCDNet releases weights exclusively for KITTI-360, and BecPlace++ provides a reproducible training recipe on KITTI. We benchmark our method against BecPlace++ on KITTI-02 and against LCDNet on KITTI-360-00, thereby adhering to the publicly available model domains. As shown, our method surpasses LCDNet on KITTI-360-00 while remaining marginally behind BEV-

TABLE III
PERFORMANCE COMPARISON ON LONG-TERM SEQUENCES (AUC ↑ /
MAX F1 SCORE ↑)

Method	NCLT		MulRan	
	L1	L2	L1	L2
M2DP	0.23/0.35	0.25/0.39	0.09/0.22	0.08/0.25
NDT	0.30/0.39	0.31/0.45	0.22/0.38	0.10/0.23
SC++	0.49/0.57	0.39/0.49	0.29/0.45	0.18/0.34
STD	0.51/0.54	0.50/0.57	0.33/0.45	0.27/0.41
Ours	0.75/0.77	0.70/0.73	0.38/0.51	0.35/0.48

Note: On the left is the AUC and on the right is the max F1 score. The best-performing method is bolded. "NCLT-L1" and "NCLT-L2" represent "2012-03-17" to "2012-02-04" and "2012-08-20" to "2012-02-04", respectively. MulRan-L1, and "MulRan-L2" represent "Sejong02" to "Sejong01", and "Sejong03" to "Sejong01", respectively.

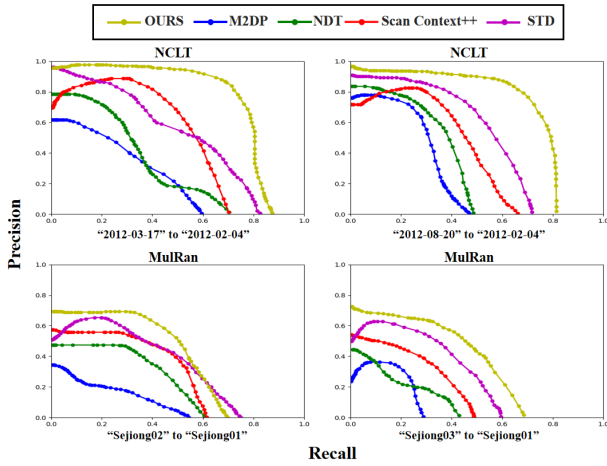


Fig. 8. Precision–recall curve NCLT, MulRan on long-term.

Place++ on KITTI-02, particularly at higher recall regions. This clarifies the contexts in which our approach's performance is slightly lower, corroborating both its strong empirical efficacy and its untapped potential.

As demonstrated, our method surpasses comparative approaches for four reasons. First, our implicit representation enhances BEV uniformity, producing more consistent spatial descriptors. Second, we integrate information from multiple modalities at both macro and micro scales, then fuse them geometrically, resulting in a richer and more hierarchical understanding of the environment. Third, our geometric descriptors disregard redundant ground-level data and focus on distinctive features, such as edges and corners, marking a clear methodological difference. Finally, the implicit representation suppresses dynamic elements, effectively reducing noise interference.

D. Ablation Study

To analyze the contributions of individual method components to place recognition performance, we designed ablation experiments. Specifically, we examined whether including the

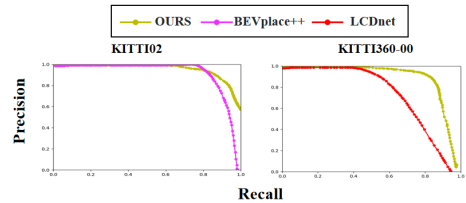


Fig. 9. Precision–recall curve KITTI02, KITTI360-00 on learning-based method.

implicit neural representation, as well as the BEV and normal vector modules, affected 3D place recognition accuracy.

To validate the contribution of the point-based implicit representation to our place recognition framework, we conducted two experimental configurations on our dataset. The first configuration retained all default parameters. The second configuration removed the implicit representation module. Without an implicit submap, we used a voxelization-based statistical method to generate occupancy grids for standard submaps. We calculated the point density within each voxel and set a density threshold that matched that of the implicit submaps. This ensured resolution consistency. For normal vector estimation, we used a principal component analysis (PCA)-based approach. PCA was computed on each point's local neighborhood. The eigenvector with the smallest eigenvalue was designated as the surface normal. Ablation tests were conducted across four datasets, encompassing both short-term and long-term scenarios. Quantitative results (AUC and Maximum F1-score) for all datasets are summarized in Table IV.

Building on the implicit submap representation, we conducted two additional experiments. One used only BEV features, while the other used only normal vector features. Detailed quantitative comparisons are provided in Table IV. As shown in the table, removing the implicit submap representation leads to significant performance degradation. This decline is due mainly to two sources: errors in surface normal estimation and inaccuracies in occupancy grid generation. Both introduce noise that compromises 3D place recognition robustness. The results also show that macro-level BEV information and local micro-scale information from the main 3D segments work together to produce a robust descriptor.

E. Computational Cost and Storage Efficiency

We conducted comparative experiments on the runtime of our method to demonstrate its efficiency in 3D place recognition. We statistically analyzed the average time required to generate descriptors for each submap across all sequences. For the three most critical components, we calculated their average times separately and compared our method with other approaches. The running time of our method was calculated by measuring the times required for descriptor generation and retrieval. The results are presented in Table V. From the table, we can see that our method is not inferior to most methods in terms of running time, even when using implicit expressions. Our implicit representation is lightweight and efficient. We use the Voxel Hashing technique to efficiently index nerve

TABLE IV
ABLATION STUDY RESULTS: AUC ↑ AND MAX F1 ↑ SCORES ACROSS DATASETS

Components			KITTI	KITTI-360	NCLT	Mulran
Implicit Rep.	BEV Image	Normal Vector	(AUC / F1)	(AUC / F1)	(AUC / F1)	(AUC / F1)
✓	✓	✓	0.91 / 0.86	0.85 / 0.84	0.80 / 0.79	0.51 / 0.60
		✓	0.59 / 0.57	0.50 / 0.48	0.47 / 0.42	0.32 / 0.27
✓	✓		0.76 / 0.79	0.75 / 0.77	0.73 / 0.71	0.42 / 0.40
✓		✓	0.81 / 0.79	0.72 / 0.73	0.76 / 0.78	0.48 / 0.50

Note: The best performance for each dataset is highlighted in bold. Results are presented as AUC score / Max F1 score.

TABLE V
TIME CONSUMPTION (MS) OF DIFFERENT METHODS

Method	KITTI	KITTI360	NCLT	MulRan
M2DP	73.2	74.1	80.2	76.2
NDT	465.2	451.2	387.2	392.1
SC++	62.1	59.4	57.2	63.1
STD	38.2	33.2	36.9	40.1
Ours	60.2	71.3	63.4	62.8
Ours(no implicit)	31.6	37.2	33.9	35.2
Ours(only implicit)	28.6	34.2	29.5	27.6

TABLE VI
MEMORY CONSUMPTION IN MB

Method	Raw point cloud	Ours
KITTI02	9002.3	90.1(1.0%)
KITTI06	2052.2	18.58(0.9%)
KITTI360-00	21210.3	255.3(1.1%)
NCLT02	15366	108.2(0.07%)

points and reduce unnecessary optimization iterations. Our segmentation of the major 3D segments is also fast and efficient. Finally, our method achieves real-time performance.

We further demonstrate the storage efficiency advantage conferred by our implicit neural-point representation factor. Prior work often focuses solely on descriptor extraction while retaining raw point-cloud formats for downstream map fusion and maintenance. On several representative sequences, we quantify the compression ratio between our implicit encoding and the raw point clouds. Table VI shows that our representation yields substantial storage savings. This advantage unlocks significant potential for subsequent map-merging and edge-cloud collaborative mapping tasks.

V. CONCLUSION

In this paper, we propose a novel 3D place recognition method inspired by implicit representations. The method begins by acquiring only occupancy grids, uniform triangular points, and globally consistent normal vectors. Submap-based implicit representations are leveraged to process this information. The data is then used to generate BEV images and information on clustered 3D segments. We employ Log-Gabor filters to derive descriptors for the BEV images. We also compute descriptors for the 3D segments using the angular differences between their normal vectors. By concatenating these two descriptors, we construct a cross-modal geometric

hierarchy fusion feature. To our knowledge, this is the first framework to introduce cross-modal geometric features for 3D place recognition. It leverages the expressive power of implicit representations to establish a new performance frontier.

In future work, we will further explore the possibilities and roles of implicit representations in place recognition. This includes developing new representation paradigms specifically tailored for this task. Additionally, we note that the current method has not been evaluated under a unified dataset benchmark. We aim to construct a large-scale, standardized dataset that unifies and facilitates fair comparisons across different environments. Based on this unified benchmark, we will also attempt to design an end-to-end place recognition framework fully based on implicit representations.

REFERENCES

- [1] Du Z, Ji S, Khoshelham K. 3D LiDAR-Based Place Recognition Techniques: A Review of the Past 10 Years[J]. IEEE Transactions on Instrumentation and Measurement, 2024.
- [2] Wu Z, Wang W, Zhang J, et al. Global localization in repetitive and ambiguous environments[C]//2023 IEEE International Conference on Robotics and Automation (ICRA). IEEE, 2023: 12374-12380.
- [3] Liso L, Sandström E, Yugay V, et al. Loopy-slam: Dense neural slam with loop closures[C]//Proceedings of the IEEE/CVF Conference on Computer Vision and Pattern Recognition. 2024: 20363-20373.
- [4] Lim H, Kim B, Kim D, et al. Quattro++: Robust global registration exploiting ground segmentation for loop closing in LiDAR SLAM[J]. The International Journal of Robotics Research, 2024, 43(5): 685-715.
- [5] Liu K, Cao M. Dlc-slam: A robust lidar-slam system with learning-based denoising and loop closure[J]. IEEE/ASME Transactions on Mechatronics, 2023, 28(5): 2876-2884.
- [6] Yu S, Fu C, Gostar A K, et al.. A review on map-merging methods for typical map types in multiple-ground-robot SLAM solutions[J]. Sensors, 2020, 20(23): 6988.
- [7] Zhou B, He Y, Huang W, et al. Place recognition and navigation of outdoor mobile robots based on random Forest learning with a 3D LiDAR[J]. Journal of Intelligent and Robotic Systems, 2022, 104(4): 72.
- [8] Suomela L, Kalliola J, Edelman H, et al. Placenav: Topological navigation through place recognition[C]//2024 IEEE International Conference on Robotics and Automation (ICRA). IEEE, 2024: 5205-5213.
- [9] Gupta S, Guadagnino T, Mersch B, et al. Effectively detecting loop closures using point cloud density maps[C]//2024 IEEE International Conference on Robotics and Automation (ICRA). IEEE, 2024: 10260-10266.
- [10] Hui L, Yang H, Cheng M, et al. Pyramid point cloud transformer for large-scale place recognition[C]//Proceedings of the IEEE/CVF International Conference on Computer Vision. 2021: 6098-6107.
- [11] Vidanapathirana K, Moghadam P, Harwood B, et al. Locus: Lidar-based place recognition using spatiotemporal higher-order pooling[C]//2021 IEEE International Conference on Robotics and Automation (ICRA). IEEE, 2021: 5075-5081.
- [12] Shan T, Englot B, Duarte F, et al. Robust place recognition using an imaging lidar[C]//2021 IEEE international conference on robotics and automation (ICRA). IEEE, 2021: 5469-5475.

- [13] Jiang B, Shen S. Contour context: Abstract structural distribution for 3d lidar loop detection and metric pose estimation[C]//2023 IEEE international conference on robotics and automation (ICRA). IEEE, 2023: 8386-8392.
- [14] Zhang Z, Huang Y, Si S, et al. Osk: A novel lidar occupancy set key-based place recognition method in urban environment[J]. IEEE Transactions on Instrumentation and Measurement, 2024.
- [15] Dube R, Cramariuc A, Dugas D, et al. SegMap: Segment-based mapping and localization using data-driven descriptors[J]. The International Journal of Robotics Research, 2020, 39(2-3): 339-355.
- [16] Lai H, Yin P, Scherer S. Adafusion: Visual-lidar fusion with adaptive weights for place recognition[J]. IEEE Robotics and Automation Letters, 2022, 7(4): 12038-12045.
- [17] Uy M A, Lee G H. Pointnetvlad: Deep point cloud based retrieval for large-scale place recognition[C]//Proceedings of the IEEE conference on computer vision and pattern recognition. 2018: 4470-4479.
- [18] Yuan C, Lin J, Zou Z, et al. Std: Stable triangle descriptor for 3d place recognition[C]//2023 IEEE international conference on robotics and automation (ICRA). IEEE, 2023: 1897-1903.
- [19] Guo J, Borges P V K, Park C, et al. Local descriptor for robust place recognition using lidar intensity[J]. IEEE Robotics and Automation Letters, 2019, 4(2): 1470-1477.
- [20] Vidanapathirana K, Ramezani M, Moghadam P, et al. LoGG3D-Net: Locally guided global descriptor learning for 3D place recognition[C]//2022 International Conference on Robotics and Automation (ICRA). IEEE, 2022: 2215-2221.
- [21] Luo L, Zheng S, Li Y, et al. BEVPlace: Learning LiDAR-based place recognition using bird's eye view images[C]//Proceedings of the IEEE/CVF International Conference on Computer Vision. 2023: 8700-8709.
- [22] Xu D, Liu J, Hyppä J, et al. A heterogeneous 3D map-based place recognition solution using virtual LiDAR and a polar grid height coding image descriptor[J]. ISPRS Journal of Photogrammetry and Remote Sensing, 2022, 183: 1-18.
- [23] Di Giannarino L, Aloise I, Stachniss C, et al. Visual place recognition using lidar intensity information[C]//2021 IEEE/RSJ International Conference on Intelligent Robots and Systems (IROS). IEEE, 2021: 4382-4389.
- [24] Siva S, Nahman Z, Zhang H. Voxel-based representation learning for place recognition based on 3d point clouds[C]//2020 IEEE/RSJ International Conference on Intelligent Robots and Systems (IROS). IEEE, 2020: 8351-8357.
- [25] Wang S, Li H, Miao T, et al. Feature Extraction of Horizontal Plane and Optimization of 3D LiDAR SLAM in Indoor Environments[J]. IEEE Transactions on Instrumentation and Measurement, 2025.
- [26] Tang H, Niu X, Zhang T, et al. LE-VINS: A robust solid-state-LiDAR-enhanced visual-inertial navigation system for low-speed robots[J]. IEEE Transactions on Instrumentation and Measurement, 2023, 72: 1-13.
- [27] Zou Q, Sun Q, Chen L, et al. A comparative analysis of LiDAR SLAM-based indoor navigation for autonomous vehicles[J]. IEEE Transactions on Intelligent Transportation Systems, 2021, 23(7): 6907-6921.
- [28] Ruan J, Li B, Wang Y, et al. Slamesh: Real-time lidar simultaneous localization and meshing[C]//2023 IEEE International Conference on Robotics and Automation (ICRA). IEEE, 2023: 3546-3552.
- [29] Niu L, Wang Z, Lin Z, et al. Voxel-Based Navigation: A Systematic Review of Techniques, Applications, and Challenges[J]. ISPRS International Journal of Geo-Information, 2024, 13(12): 461.
- [30] Ren Y, Cai Y, Zhu F, et al. Rog-map: An efficient robocentric occupancy grid map for large-scene and high-resolution lidar-based motion planning[C]//2024 IEEE/RSJ International Conference on Intelligent Robots and Systems (IROS). IEEE, 2024: 8119-8125.
- [31] Mildenhall B, Srinivasan P P, Tancik M, et al. Nerf: Representing scenes as neural radiance fields for view synthesis[J]. Communications of the ACM, 2021, 65(1): 99-106.
- [32] Mescheder L, Oechsle M, Niemeyer M, et al. Occupancy networks: Learning 3d reconstruction in function space[C]//Proceedings of the IEEE/CVF conference on computer vision and pattern recognition. 2019: 4460-4470.
- [33] Park J J, Florence P, Straub J, et al. Deep sdf: Learning continuous signed distance functions for shape representation[C]//Proceedings of the IEEE/CVF conference on computer vision and pattern recognition. 2019: 165-174.
- [34] Xu Q, Xu Z, Philip J, et al. Point-nerf: Point-based neural radiance fields[C]//Proceedings of the IEEE/CVF conference on computer vision and pattern recognition. 2022: 5438-5448.
- [35] Müller T, Evans A, Schied C, et al. Instant neural graphics primitives with a multiresolution hash encoding[J]. ACM transactions on graphics (TOG), 2022, 41(4): 1-15.
- [36] Takikawa T, Litalien J, Yin K, et al. Neural geometric level of detail: Real-time rendering with implicit 3d shapes[C]//Proceedings of the IEEE/CVF conference on computer vision and pattern recognition. 2021: 11358-11367.
- [37] Azinović D, Martin-Brualla R, Goldman D B, et al. Neural rgb-d surface reconstruction[C]//Proceedings of the IEEE/CVF Conference on Computer Vision and Pattern Recognition. 2022: 6290-6301.
- [38] Sucar E, Liu S, Ortiz J, et al. imap: Implicit mapping and positioning in real-time[C]//Proceedings of the IEEE/CVF international conference on computer vision. 2021: 6229-6238.
- [39] Johari M M, Carta C, Fleuret F. Eslam: Efficient dense slam system based on hybrid representation of signed distance fields[C]//Proceedings of the IEEE/CVF Conference on Computer Vision and Pattern Recognition. 2023: 17408-17419.
- [40] Wang H, Wang J, Agapito L. Co-slam: Joint coordinate and sparse parametric encodings for neural real-time slam[C]//Proceedings of the IEEE/CVF Conference on Computer Vision and Pattern Recognition. 2023: 13293-13302.
- [41] Zhu Z, Peng S, Larsson V, et al. Nice-slam: Neural implicit scalable encoding for slam[C]//Proceedings of the IEEE/CVF conference on computer vision and pattern recognition. 2022: 12786-12796.
- [42] Kuang H, Chen X, Guadagnino T, et al. Ir-mcl: Implicit representation-based online global localization[J]. IEEE Robotics and Automation Letters, 2023, 8(3): 1627-1634.
- [43] Wiesmann L, Guadagnino T, Vizzo I, et al. Locndf: Neural distance field mapping for robot localization[J]. IEEE Robotics and Automation Letters, 2023, 8(8): 4999-5006.
- [44] Zhong X, Pan Y, Behley J, et al. Shine-mapping: Large-scale 3d mapping using sparse hierarchical implicit neural representations[C]//2023 IEEE International Conference on Robotics and Automation (ICRA). IEEE, 2023: 8371-8377.
- [45] Isaacson S, Kung P C, Ramanagopal M, et al. Loner: Lidar only neural representations for real-time slam[J]. IEEE Robotics and Automation Letters, 2023, 8(12): 8042-8049.
- [46] Deng J, Wu Q, Chen X, et al. Nerf-loam: Neural implicit representation for large-scale incremental lidar odometry and mapping[C]//Proceedings of the IEEE/CVF International Conference on Computer Vision. 2023: 8218-8227.
- [47] Pan Y, Zhong X, Wiesmann L, et al. PIN-SLAM: LiDAR SLAM using a point-based implicit neural representation for achieving global map consistency[J]. IEEE Transactions on Robotics, 2024.
- [48] Rusu R B, Blodow N, Marton Z C, et al. Aligning point cloud views using persistent feature histograms[C]//2008 IEEE/RSJ international conference on intelligent robots and systems. IEEE, 2008: 3384-3391.
- [49] Rusu R B, Blodow N, Beetz M. Fast point feature histograms (FPFH) for 3D registration[C]//2009 IEEE international conference on robotics and automation. IEEE, 2009: 3212-3217.
- [50] Salti S, Tombari F, Di Stefano L. SHOT: Unique signatures of histograms for surface and texture description[J]. Computer vision and image understanding, 2014, 125: 251-264.
- [51] Johnson A E, Hebert M. Using spin images for efficient object recognition in cluttered 3D scenes[J]. IEEE Transactions on pattern analysis and machine intelligence, 1999, 21(5): 433-449.
- [52] Muhammad N, Lacroix S. Loop closure detection using small-sized signatures from 3D LIDAR data[C]//2011 IEEE International Symposium on Safety, Security, and Rescue Robotics. IEEE, 2011: 333-338.
- [53] Röhling T, Mack J, Schulz D. A fast histogram-based similarity measure for detecting loop closures in 3-d lidar data[C]//2015 IEEE/RSJ international conference on intelligent robots and systems (IROS). IEEE, 2015: 736-741.
- [54] He L, Wang X, Zhang H. M2DP: A novel 3D point cloud descriptor and its application in loop closure detection[C]//2016 IEEE/RSJ International Conference on Intelligent Robots and Systems (IROS). IEEE, 2016: 231-237.
- [55] Kim G, Kim A. Scan context: Egocentric spatial descriptor for place recognition within 3d point cloud map[C]//2018 IEEE/RSJ International Conference on Intelligent Robots and Systems (IROS). IEEE, 2018: 4802-4809.
- [56] Kim G, Choi S, Kim A. Scan context++: Structural place recognition robust to rotation and lateral variations in urban environments[J]. IEEE Transactions on Robotics, 2021, 38(3): 1856-1874.
- [57] Wang H, Wang C, Xie L. Intensity scan context: Coding intensity and geometry relations for loop closure detection[C]//2020 IEEE international conference on robotics and automation (ICRA). IEEE, 2020: 2095-2101.
- [58] Ou F, Li Y, Miao Z. Place recognition of large-scale unstructured orchards with attention score maps[J]. IEEE Robotics and Automation Letters, 2023, 8(2): 958-965.

- [59] Wang Y, Sun Z, Xu C Z, et al. Lidar iris for loop-closure detection[C]//2020 IEEE/RSJ International Conference on Intelligent Robots and Systems (IROS). IEEE, 2020: 5769-5775.
- [60] Qi C R, Su H, Mo K, et al. Pointnet: Deep learning on point sets for 3d classification and segmentation[C]//Proceedings of the IEEE conference on computer vision and pattern recognition. 2017: 652-660.
- [61] Arandjelovic R, Gronat P, Torii A, et al. NetVLAD: CNN architecture for weakly supervised place recognition[C]//Proceedings of the IEEE conference on computer vision and pattern recognition. 2016: 5297-5307.
- [62] Xia Y, Xu Y, Li S, et al. SOE-Net: A self-attention and orientation encoding network for point cloud based place recognition[C]//Proceedings of the IEEE/CVF Conference on computer vision and pattern recognition. 2021: 11348-11357.
- [63] Zhang W, Xiao C. PCAN: 3D attention map learning using contextual information for point cloud based retrieval[C]//Proceedings of the IEEE/CVF conference on computer vision and pattern recognition. 2019: 12436-12445.
- [64] Vidanapathirana K, Moghadam P, Harwood B, et al. Locus: Lidar-based place recognition using spatiotemporal higher-order pooling[C]//2021 IEEE International Conference on Robotics and Automation (ICRA). IEEE, 2021: 5075-5081.
- [65] Hou Z, Yan Y, Xu C, et al. Hitpr: Hierarchical transformer for place recognition in point cloud[C]//2022 International Conference on Robotics and Automation (ICRA). IEEE, 2022: 2612-2618.
- [66] Vaswani A, Shazeer N, Parmar N, et al. Attention is all you need[J]. Advances in neural information processing systems, 2017, 30.
- [67] Kim G, Park B, Kim A. 1-day learning, 1-year localization: Long-term lidar localization using scan context image[J]. IEEE Robotics and Automation Letters, 2019, 4(2): 1948-1955.
- [68] Li L, Kong X, Zhao X, et al. SSC: Semantic scan context for large-scale place recognition[C]//2021 IEEE/RSJ International Conference on Intelligent Robots and Systems (IROS). IEEE, 2021: 2092-2099.
- [69] Liu Z, Zhou S, Suo C, et al. Lpd-net: 3d point cloud learning for large-scale place recognition and environment analysis[C]//Proceedings of the IEEE/CVF international conference on computer vision. 2019: 2831-2840.
- [70] Qiao Z, Hu H, Shi W, et al. A registration-aided domain adaptation network for 3D point cloud based place recognition[C]//2021 IEEE/RSJ International Conference on Intelligent Robots and Systems (IROS). IEEE, 2021: 1317-1322.
- [71] Wang S, Zhang Y, Zhang J, et al. Density-Driven Adaptive Hybrid Network for Large-Scale Place Recognition[J]. IEEE Transactions on Instrumentation and Measurement, 2025.
- [72] Zermas D, Izzat I, Papanikolopoulos N. Fast segmentation of 3D point clouds: A paradigm on LiDAR data for autonomous vehicle applications[C]//2017 IEEE International Conference on Robotics and Automation (ICRA). IEEE, 2017: 5067-5073.
- [73] Cao Y, Wang Y, Xue Y, et al. FEC: Fast Euclidean clustering for point cloud segmentation[J]. Drones, 2022, 6(11): 325.
- [74] Jégou H, Douze M, Schmid C, et al. Aggregating local descriptors into a compact image representation[C]//2010 IEEE computer society conference on computer vision and pattern recognition. IEEE, 2010: 3304-3311.
- [75] Fischer S, Šroubek F, Perrinet L, et al. Self-invertible 2D log-Gabor wavelets[J]. International Journal of Computer Vision, 2007, 75: 231-246.
- [76] Li J, Hu Q, Ai M. RIFT: Multi-modal image matching based on radiation-variation insensitive feature transform[J]. IEEE Transactions on Image Processing, 2019, 29: 3296-3310.
- [77] Geiger A, Lenz P, Urtasun R. Are we ready for autonomous driving? the kitti vision benchmark suite[C]//2012 IEEE conference on computer vision and pattern recognition. IEEE, 2012: 3354-3361.
- [78] Liao Y, Xie J, Geiger A. Kitti-360: A novel dataset and benchmarks for urban scene understanding in 2d and 3d[J]. IEEE Transactions on Pattern Analysis and Machine Intelligence, 2022, 45(3): 3292-3310.
- [79] Carlevaris-Bianco N, Ushani A K, Eustice R M. University of Michigan North Campus long-term vision and lidar dataset[J]. The International Journal of Robotics Research, 2016, 35(9): 1023-1035.
- [80] Kim G, Park Y S, Cho Y, et al. Mulran: Multimodal range dataset for urban place recognition[C]//2020 IEEE international conference on robotics and automation (ICRA). IEEE, 2020: 6246-6253.
- [81] Magnusson M, Andreasson H, Nüchter A, et al. Automatic appearance-based loop detection from three-dimensional laser data using the normal distributions transform[J]. Journal of Field Robotics, 2009, 26(11-12): 892-914.
- [82] Cui Y, Chen X, Zhang Y, et al. Bow3d: Bag of words for real-time loop closing in 3d lidar slam[J]. IEEE Robotics and Automation Letters, 2022, 8(5): 2828-2835.
- [83] Xu X, Lu S, Wu J, et al. Ring++: Roto-translation invariant gram for global localization on a sparse scan map[J]. IEEE Transactions on Robotics, 2023, 39(6): 4616-4635.
- [84] Cattaneo D, Vaghi M, Valada A. Lcdnet: Deep loop closure detection and point cloud registration for lidar slam[J]. IEEE Transactions on Robotics, 2022, 38(4): 2074-2093.
- [85] Luo L, Cao S Y, Li X, et al. Bevplace++: Fast, robust, and lightweight lidar global localization for unmanned ground vehicles[J]. IEEE Transactions on Robotics, 2025.